Microchimica Acta (2020) 187:62
https://doi.org/10.1007/s00604-019-3987-3

ORIGINAL PAPER

# Fabrication of $WO_2$/W@C core-shell nanospheres for voltammetric simultaneous determination of thymine and cytosine

Qiong Wang[1] · Jing Zhang[1] · Qi Li[1] · Xingjia Guo[1] · Lei Zhang[1]

Received: 20 June 2019 / Accepted: 28 October 2019


## Abstract

Pomegranate-like multicore $WO_2$/W nanocrystals wrapped with layers of multiporous carbon were fabricated via carbonization of a copper(II)-organic framework host and a tungsten-based polyoxometalates guest, and subsequent etching off the metallic copper. The $WO_2$/W@C core-shell nanospheres were employed to modify an electrode for the analysis of the DNA bases thymine (T) and cytosine (C) by differential pulse voltammetry. The $WO_2$/W@C exhibited strongly increased oxidation signal of T and C. Under optimized conditions, the enhanced peak current represented excellent analytical performance for determination of T and C. This is attributed to the synergic effects of the porous multicore–shell microstructure and the use of tungsten-based materials with their excellent electrocatalytic activity for T and C, with typical peaks voltages near 1.26 V and 1.44 V. The calibration plots for T and C extend from 1 to 4000 μM and from 1 to 3000 μM, respectively, and both detection limits are 0.2 μM. The method was successfully applied to the determination of T and C in spiked blood and urine samples, and the recoveries are form 97.3 to 105.0%.

**Keywords** Multicore–shell $WO_2$/W@C · Biosensor · Simultaneous determination · Oxygen vacancies

## Introduction

It is important to quantify the number of pyrimidine bases in DNA [1, 2]. Generally, several methods including mass spectrometry, chemiluminescence, spectroscopic methods, and high performance liquid chromatography have been used for determination of T and C [3, 4]. Electrochemical methods are widely employed on account of their low cost, distinguished sensitivity, and easy to realize miniaturization [5]. However, simultaneous detection of T and C still faces numerous challenges, such as the two oxidation peaks of T and C possess higher overpotential and also tend to overlap. Many electrode materials do not give a response signal or generate insensitive peak signal. Consequently, there are little literatures on the electrochemical simultaneous detection of T and C. Thus, genuine designing a modified material is a challenge to overcome the above difficulties.

The metallic (such as Ni, Co, Au and Pt) nanoparticles (NPs) based on active substrates, on behalf of significant type of electrochemistry catalysts to detect DNA [6], led to extensive and intensive investigation. However, the metallic NPs is often to form aggregation state within metallic catalysts due to relatively weak interaction between the substrates and the metallic NPs, which tends to show unsatisfactory sensitivity, restricted activity, and instability. Recent studies reported that carbon materials, such as carbon nanotubes [7], mesoporous carbon fibers [8], ionic liquids@carbon compounds [9], have been developed to detect T and C. It has been confirmed that metallic NPs inside carbon architectures can improve the electron and charge transport, and enhance catalytic

**Electronic supplementary material** The online version of this article (https://doi.org/10.1007/s00604-019-3987-3) contains supplementary material, which is available to authorized users.

✉ Xingjia Guo
guoxja@sina.com

✉ Lei Zhang
zhanglei63@126.com

[1] College of Chemistry, Liaoning University, 66 Chong shan Middle Road, Shenyang, Liaoning 110036, People's Republic of China

Published online: 18 December 2019

activity towards electrochemical reactions [10, 11]. Hence, the reasonably designing and structuring a hybrid as new charming electrode material is required to improve the analytical performance of electrochemical DNA sensor. The good performance of metal-implanted carbon nanostructures prompted us to consider whether a metal/carbon-based nanomaterial may be designed as reliable catalyst for detection of T and C.

Tungsten and tungsten oxide have aroused researchers' favor because of their excellent catalytic activity and good conductivity, as well as their environmental friendliness and abundant resources. However, the application of W or $WO_2$ NPs faces a thorny challenge. They undergo irreversible aggregation and fusion at high temperatures. In consequence, fabricated W or $WO_2$ nanostructure with luxuriantly exposed active sites and high porosity is urgent. The shell-core structure being consisted of multihole organic shell and encapsulated catalytic NPs core has caused wide concern, the organic framework (shell) made for NPs dispersion, also prevent them from clumping and sintering, the reactants diffused in the porous channel reducing the spread pathways and exposing more metal catalytic sites [12–17]. Especially, the oxygen vacancies (OVs) as active sites generated in the composite can also enhance the electrocatalysis activities [18, 19].

Herein, a method incorporated one step hydrothermal process, carburization reaction and a follow-up etching step were used to obtain ultrafine $WO_2$/W nanoparticles encapsulated carbon sphere ($WO_2$/W@C). The pomegranate-like multicore–shell $WO_2$/W porous carbon spheres are composed of well-proportioned conjoined carbon layers on the outer surface (outer shell) and interconnected carbon nanospheres (inner shell), forming a characteristic multicore–shell structure. These characteristics endow $WO_2$/W@C with greatly improved electrochemical properties. Benifiting from the synergistic effect of the ultrafine primary $WO_2$/W nanocrystallites, the porosity and novel structure as well as OVs make the composite possess more catalytic active sites and the core-shell structure foster an excellent electrocatalytic activity for simultaneous detecting T and C.

## Reagents and materials

Copper(II) acetate monohydrate ($Cu(CH_3COO)_2{\cdot}H_2O$, 99.9%), phosphotungstic acid hydrate ($H_3W_{12}O_{40}P{\cdot}xH_2O$), $FeCl_3$(99.9%), trimesic acid ($H_3BTC$ 95%), sodium hydrate(95%), L-glutamic acid ($C_5H_9NO_4$, 99.9%), aceticacid (95%), 5% Nafion ethanol solution (D520), sodium acetate (95%), thymine (T, ≥ 99.7%) and cytosine (C, ≥ 99.5), ethanol were purchased from Sinopharm Chemical Reagent Co. Ltd. (Shanghai, China, www.sinoreagent.com). The supporting electrolyte solution (phosphate buffer (PB)) was composed of 0.2 M $Na_2HPO_4$-$NaH_2PO_4$ (pH 5.0).

## Apparatus and instruments

The microstructures and morphologies of samples were characterized by scanning electron microscopy (SEM, Hitachi SU8000) attached with an energy-dispersive X-ray spectroscopy (EDX) and transmission electron microscopy (TEM, JEOL JEM-2100, Japan). X-ray photoelectron spectroscopic (XPS, Thermo Electron, ESCALAB 250 Xi., USA) data were obtained at 293 K. The chamber pressure was kept below $10^{-8}$ Torr. A binding energy of 284.8 eV for the C 1 s level was used as an internal reference. The C1s peaks were deconvoluted using XPS Peak 4.1. X-ray diffraction patterns were recorded on X-ray diffractometer (XRD, Siemens D5000, Germany) at 150 mA and 40 kV with Cu Kα radiation. Laser Confocal Micro Raman Spectroscope (Raman, HORIBA, LabRAM XploRA, France). A CHI660D electrochemical workstation (Shanghai Chen Hua Instruments Co. China) was selected for electrochemical measurements coupled with a conventional three-electrode cell.

## Synthesis of electrode materials

**Synthesis of W-Cu-MOF nanosphere** Based on the method reported by Wu et al., we synthesis of W-Cu-MOF nanosphere with some modifications. [20]. Typically, 0.47 g of $H_3W_{12}O_{40}P{\cdot}xH_2O$, 0.07 g of $C_5H_9NO_4$ and 0.2 g of $Cu(CH_3COO)_2{\cdot}H_2O$ were mixed with 40 mL of deionized water, and then stirred until completely dissolved. Afterwards, 0.03 g of $H_3BTC$ was absolutely dissolved in 40 mL ethanol, and then slowly poured into the above solution with stirring. On account of forming W-Cu-MOF nanocrystals, the solution turned turbidity in the turn of a hand. After stirring for 14 h at room temperature, the green sediment was collected by centrifugation and rinsed with water and ethanol. The product was dried at 60 °C overnight.

**Synthesis of porous $WO_2$/W@C nanosphere** The W-Cu-MOF nanosphere was annealed in a pipe furnace with a ramp rate of 5 °C·min$^{-1}$ under $N_2$ flow, and held at 800 °C for 6 h. The samples were obtained as Cu-$WO_2$/W@C which were dispersed in 0.15 M $FeCl_3$ aqueous solution and kept stirring 3 h to etch Cu nanoparticles. The yielding porous $WO_2$/W@C nanospheres were collected through washing with water for 5 times, and then dried at 80 °C overnight. The annealed temperature keep at 600 °C, 700 °C and 900 °C were labeled as $WO_3$/$WO_{2.83}$@C, $WO_{2.83}$@C and W/$WO_2$@C, respectively. The total preparation process diagram of pomegranate-like multicore–shell $WO_2$/W@C is particularly described and schematically illustrated in Fig. 1.

**Synthesis of Cu-MOF nanosphere** For comparison, Cu-MOF was synthesized by using a similar method, excepting that the phosphomolybdic acid hydrate was not added to the reaction.

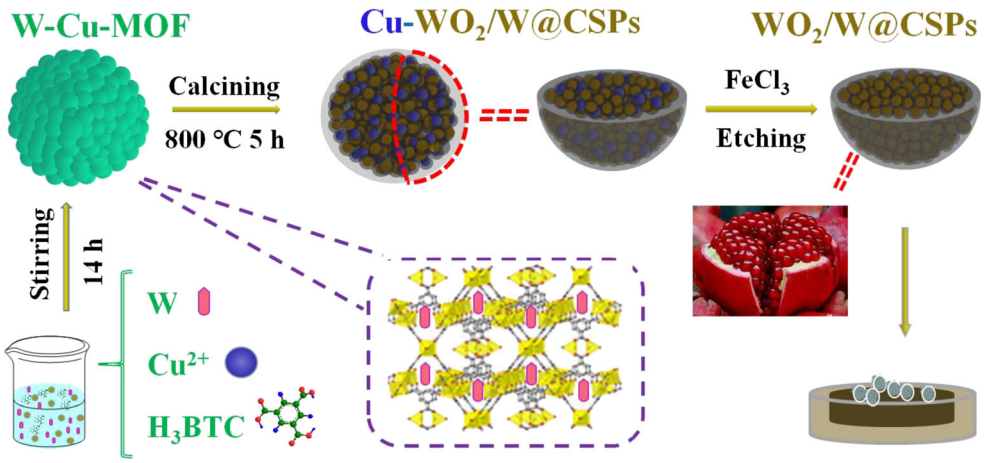


**Fig. 1** The typical fabricated process of $WO_2$/W@C/GCE electrode

**Synthesis of Cu@C nanosphere** The Cu-MOF nanospheres were synthesized by annealed Cu-MOF using the same procedure with $Mo_xC$@C nanosphere.

### Fabrication of modified glassy carbon electrode (GCE)

The pretreated GCE was permitted to dry in a nitrogen stream. 6.0 mg of $WO_2$/W@C were dispersed into 2.0 mL of 5% Nafion ethanol solution and sonicated for 5 min. The 6 μL suspension was dropped onto the treated GCE with mirror-like surface and then dried in air at room temperature.

### Analytical procedure for determination of T and C

The electrochemical detections were carried out using differential pulse voltammetry (DPV) means, the DPV was performed in scanning from 0.8 V to 1.7 V in 0.2 M 5.0 mL PB, the preconcentration time was 90 s, and the accumulation potential was 0.0 V. Electrochemical impedance spectroscopy (EIS) investigation were in 0.10 M KCl solution containing $K_3[Fe(CN)_6]/K_4[Fe(CN)_6]$ (5 mM) as redox probe, and recorded at an open circuit potential with an amplitude of 5 mV over a frequency range of 0.1 Hz–$10^4$ Hz. Prior to analysis, the PB would like to be purified by nitrogen for 10 min.

### Real sample analysis

Human urine and blood serum were chose as the real sample in this experiment. The two samples were obtained from healthy volunteers at the local hospital and stored in refrigerator immediately after their collection. The human urine was centrifuged for 10 min to remove large particulate matters and filtered by nylon membrane filters, the 0.125 mL supernatant liquid was diluted with 0.2 M PB to 5 mL for sensing. The blood was added EDTA as anti-coagulant, the supernatant liquid was obtained by centrifugation and filtered by nylon membrane filters. Before measurement, the 25 μL supernatant liquid was diluted with 0.2 M PB to 5 mL for sensing. The peaks voltages of T and C are 1.26 V and 1.44 V in the DPV test.

## Results and discussion

### Choice of materials

The high overpotential is the critical problem in the detection of DNA bases group, some electroe material, such as mesoporous carbon fibers [8], ZSM-5 zeolite [9], polyaniline/$MnO_2$ [21] and ionic liquids coated $Fe_3O_4$ [22] have been reported, but the sensitivity still need to improve. Due to the inherent characteristics of transition metal, they are widely used in the electrochemical analysis and catalysis field. Among transition metals, the $WO_2$/W show obvious catalysis for the electrochemical oxidation of T/C. However, the $WO_2$/W is easily agglomerate to reduce the sensitivity of sensor. In order to improve its sensitivity, the strategy of metal-implanted carbon nanostructures was used for fabricating a new charming electrode material for the simultaneous detection of T/C. So Cu-MOF host was chosen as the substrate and W-based polyoxometalates as the guest to fabricate the pomegranate-like multicore–shell $WO_2$/W porous carbon spheres. Due to synergistic catalytic effect of porous carbon shell and $WO_2$/W core, the nanocomposite is hopeful to provide a sensitive platform for the simultaneous electrochemical determination of T/C.

### Characterization of electrode materials

The SEM images of W-Cu-MOF and $WO_2$/W@C are presented in Fig. 2a and b. The external diameter of W-Cu-MOF sphere is approximate 500 nm, and the spherical shape of $WO_2$/W@C are well kept after calcination and the removal of Cu ion process, which implied that calcination and etching made no difference on morphology, and also hint the stable

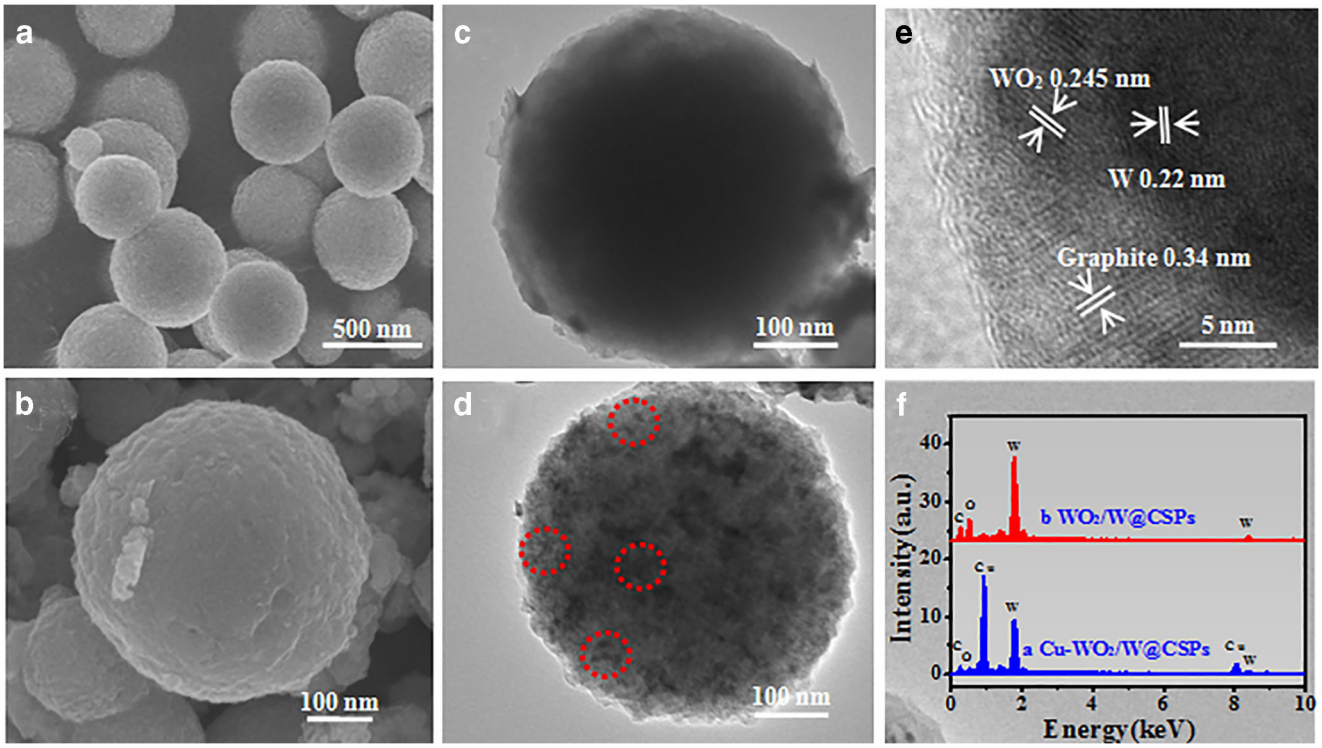


**Fig. 2** Characterization of electrode materials: SEM image of W-Cu-MOF (**a**) and $WO_2$/W@C (**b**); TEM image of Cu-$WO_2$/W@C (**c**) and $WO_2$/W@C (**d**); (**e**) HRTEM of $WO_2$/W@C (**f**) EDS patterns of Cu-$WO_2$/W@C and $WO_2$/W@C

structure derived from carbon matrix. It can be observed from the TEM image (Fig. 2c), the Cu-$WO_2$/W@C surface is coated with a carbon layer after heat treatment and no void would be found in the composite. After copper etching, $WO_2$/W@C display porous structures (Fig. 2d), all carbon nanobeads coating $WO_2$/W are well interconnected and the inner carbon nanobeads present a diameter range about 3–12 nm (in red mark). It is apparent that all the homogeneous nanobeads are well-proportioned reside in a porous carbon frame and faultlessly covered by an outer thin graphite carbon coating layer (001 plane), forming a pomegranate-like morphology. In Fig. 2e, an enlarged $WO_2$/W@C sample exhibits consummate lattice fringe with interplanar distances of 0.245 nm and 0.22 nm, which match with the d-spacing of the (110) crystal plane of $WO_2$ and W, respectively. The chemical composition of Cu-$WO_2$/W@C and $WO_2$/W@C were examined by EDX (Fig. 2f). It obviously indicates the elements in Cu-$WO_2$/W@C and $WO_2$/W@C, and also proves that $Cu^{2+}$ is removed utterly.

The crystal phase of Cu-$WO_2$/W@C, $WO_3$/$WO_{2.83}$@C, $WO_{2.83}$@C, $WO_2$/W@C and W/$WO_2$@C were characterized by XRD. In Fig. 3a, the XRD pattern confirms the pure phase purity and ideal crystallinity of Cu-$WO_2$/W@C and $WO_2$/W@C. The obvious peaks located at 25.7°, 36.8°, 37.4°, 52.9°, 53.4° and 59.9° should be attributed to (011), (002), (−202), (220), (−113) and (013) planes of $WO_2$ (PDF#32–1393) [23]. The especial peaks around 40.2°, 58.2°, 73.1° correspond to (110), (200), (211) planes of W (PDF#04–0806) [24]. The other peaks at 43.3°, 50.4° and 74.1° are correspond to (111), (200) and (220) planes of Cu (PDF#04–0836) [25]. As for $WO_2$/W@C, the Cu diffraction peaks completely disappeared, proving the copper etch successfully. Then, we evaluated the influence of calcination temperatures (Fig. 3b) in detail. At 600 °C, the $WO_{2.83}$ (PDF#36–0103) and $WO_3$ (PDF#20–1323) are generated, and then the $WO_3$ disappear as the temperature increases to 700 °C. When the temperature rises to 800 °C, the $WO_{2.83}$ is completely reduced to $WO_2$ with a small number of W, and more $WO_2$ are reduced to W while the temperature rises to 900 °C. Subsequently, we evaluated their electrochemical performance (Fig. 3c), there are only two particularly weak oxidation peaks on $WO_3$/$WO_{2.83}$@C and $WO_{2.83}$@C electrode, indicating the $WO_{2.83}$ and $WO_3$ have no catalytic activity toward electrochemical oxidation of T and C. Surprisingly, the apparent oxidation peaks are observed on $WO_2$/W@C electrode, illustrating the $WO_2$/W possesses good conductivity and electrocatalytic activity for targets. When we keep raising the temperature, the signal of oxidation peaks shows a downward trend, it may account for that carbon is consumed in the reduction process. Thus, we chose 800 °C as the optimum temperature. Raman spectra were recorded in Fig. 3d, the value of $I_D/I_G$ is 1.42, which means the presence of a large amount of disordered carbon owing to the rough structure as well as the scar after etching copper [26].

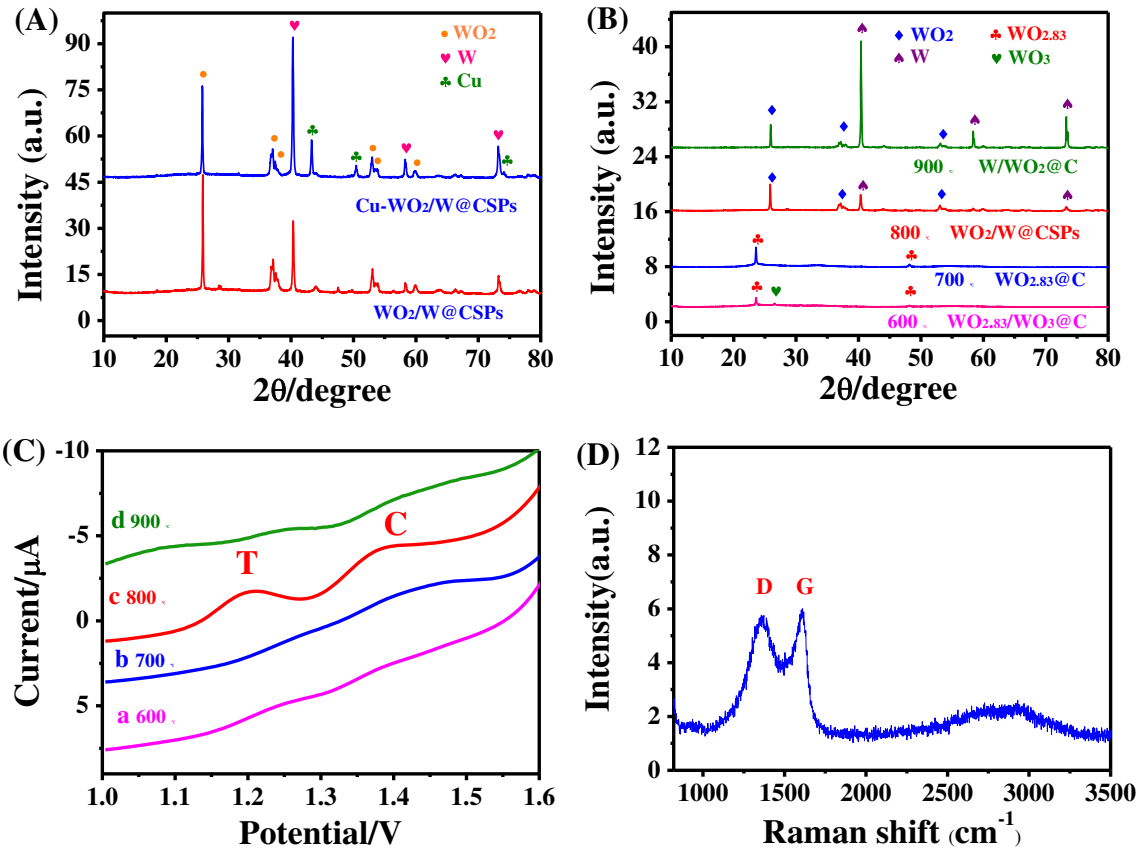


**Fig. 3** (**a**) XRD patterns of Cu-$WO_2$/W@C and $WO_2$/W@C; (**b**)XRD patterns of $WO_3$/$WO_{2.83}$@C, $WO_{2.83}$@C, $WO_2$/W@C and W/$WO_2$@C; (**c**) DPVs of the electrodes based on various pyrolysis temperature in 0.2 M PB (pH 5.5) containing 100 μM T and C; (**d**) Raman spectra of $WO_2$/W@C

The XPS analysis of $WO_2$/W@C was performed in Fig. S1, the C, W and O peaks are observed in the survey spectra (Fig. S1A). The C 1 s band (Fig. S1B) displays three primary peaks located at 288.65, 286.11 and 284.80 eV in accord with C=O, C-O and C-C/C=C bonds, respectively [27–29]. The W 4f band (Fig. S1C) shows two obvious peaks at 32.32 and 34.51 eV, which belong to W 4f 7/2 and W 4f 5/2 of $W^{4+}$, revealing that the $W^{4+}$ is derived from the reduction of $W^{6+}$ in the calcination process [30], the peak at 38.03 eV indicates the presence of metallic W. In Fig. S1D, the O 1 s band can be deconvoluted into two characteristic peaks centred at 529.70 eV (oxygen atoms bound to metals) and 531.34 eV (oxygen vacancies) [31]. The existence of oxygen vacancies may be enhance the electrocatalytic activity and surface activity of $WO_2$/W@C.

## Electrochemical characterization

The electrochemical effective surface areas of bare GCE, Cu@C/GCE, Cu-$WO_2$/W@C/GCE and $WO_2$/W@C/GCE were calculated through chronocoulometry method. The experiment was conducted in 0.1 mM $K_3[Fe(CN)_6]$ aqueous solution containing 1.0 M KCl. On the basis of the equation [32]:

$$Q(t) = \frac{2nFAcD^{1/2}t^{1/2}}{\pi^{1/2}} + Q_{dl} + Q_{ads} \quad (1)$$

where $D$ is diffusion coefficient ($7.6 \times 10^{-6}$ $cm^2 \cdot s^{-1}$), $c$ is concentration of substrate, $Q_{ads}$ is Faradaic charge, $A$ is effective areas of electrode, $Q_{dl}$ is double layer charge. Other symbols represent common meanings. As shown in Fig. 4a and b, the linear relationship Q -$t^{1/2}$ are clear described. According to the slope value, the effective area of bare GCE (a), Cu@C/GCE (b), Cu-$WO_2$/W@C/GCE (c) and $WO_2$/W@C/GCE (d) are estimated to be 0.0070 $cm^2$, 0.014 $cm^2$, 0.017 $cm^2$, and 0.035 $cm^2$, respectively. These results illustrate that the effective area of the $WO_2$/W@C/GCE is nearly 5 times as the bare GCE, which due to the multiporous nature, bumpy surface and the existence of massive oxygen vacancies on the surface of $WO_2$/W@C. Consequently exposes more abundant surface active sites and enhance the adsorption capacity, magnify the current response of targets, and improve the detection sensitivity.

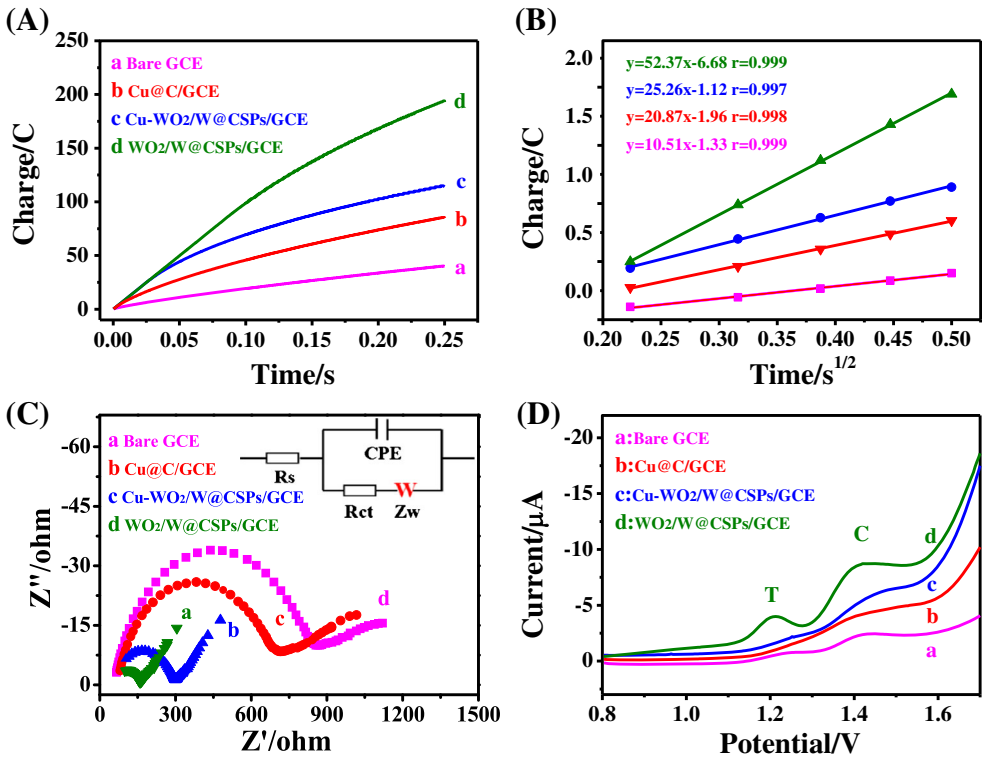


**Fig. 4** (**a**) Chronoamperometry response on various modified electrodes; (**b**) Plot of Q-$t^{1/2}$ curve; (**c**) EIS curves of various modified electrode, inset show the typical equivalent circuits; (**d**) DPVs of various modified electrodes in 0.2 M PB (pH 5.5) containing 100 μM T and C

The interfacial character of different electrodes was investigated by electrochemical impedance spectroscopy (EIS) technology. The impedance spectra of bare GCE (a), Cu@C/GCE (b), Cu-$WO_2$/W@C/GCE (c) and $WO_2$/W@C/GCE (d) are shown in the Fig. 4c. The Randles equivalence circuit model (inset of Fig. 4c) is successfully employed to fit the impedance data. In the equivalence circuit, including the resistance to electron transfer (*Rct*), the diffusion impedance (*Zw*), the interfacial capacitance (*CPE*), and the electrolyte resistance between the working and reference electrodes ($R_s$). From observation, the bare GCE has a large semicircle portion and the $R_{ct}$ value is 770 Ω, it possesses a particularly large impedance value resulting in a poor conductivity and a sluggish electron transfer rate. Compared with bare GCE, the Cu@C/GCE (630 Ω) shows a decreasing trend, revealing that the Cu@C material possesses a better electrical conductivity. After implanting W species, Cu-$WO_2$/W@C/GCE exhibits a smaller $R_{ct}$ value (260 Ω), indicating the Cu-$WO_2$/W@C possessing a faster mass transfer rate and excellent conductivity. Whereas, $WO_2$/W@C/GCE shows a minimum $R_{ct}$ value (105 Ω) after etching metallic copper. The phenomenon is mainly due to the synergistic effect. Mainly in the following aspects: the $WO_2$/W nanoparticles are conformably dispersived within carbon nanoshells and the carbon shells synchronously portray a conducting framework, in other word, multicore–shell $WO_2$/W is encapsulated within integrated porous carbon matrix and then composed nanosized carbon spheres packaged by a carbon coating layers. Such ingenious structural synergy shortens electron transport path and improves proton transfer rate. Further, in order to demonstrate the electrochemical property of various electrodes, heterogeneous electron transfer rate constant ($K_0$) was calculated based on interfacial interaction Eq. (2) [33]:

$$K_0 = \frac{RT}{n_2 F^2 A_{ec} R_{ct} C} \quad (2)$$

where, n is the electron transfer constant of the redox couple, *C* is the concentration of redox couple in the bulk solution, $A_{ec}$ is the effective area of various modified electrode, $R_{ct}$ is the charge transfer resistance, *F* is the Faraday constant, *R* is the gas constant, and *T* is the temperature. The $K_0$ value of $WO_2$/W@C/GCE ($3.68 \times 10^{-4}$ $s^{-1}$), Cu-$WO_2$/W@C/GCE ($1.49 \times 10^{-4}$ $s^{-1}$), Cu@C/GCE ($6.13 \times 10^{-5}$ $s^{-1}$) and bare GCE ($5.02 \times 10^{-5}$ $s^{-1}$) are figured out, respectively. This is the result of a strong synergistic effect between $WO_2$/W nanoparticle and closely attached carbonaceous matrix. The carbon material shortens the conduction pathway and facilitates the proton transfer on the surface of electrode.

We adopted the DPV technique to make a comparison on $WO_2$/W@C/GCE, Cu-$WO_2$/W@C/GCE, Cu@C/GCE and bare GCE in 100 μM T and C. In Fig. 4d, the obvious phenomenon is that the bare GCE exhibits two weak oxidation peaks at 1.26 V and 1.44 V. The Cu@C/GCE does not separate these two peaks and the Cu-$WO_2$/W@C/GCE has similar peak current to the bare electrode. However, the peak current

of $WO_2$/W@C/GCE show a tremendously high value and offered a prominently narrowed peak width. The peak separation of T and C was about 200 mV and the peak potential was reduced, which further declares that electric oxidation capacity was enhanced by etching metallic copper and simultaneous detection of T and C can be proceed.

## Determination of T and C

A sensitive and selective method was established based on $WO_2$/W@C/GCE for enhancing the voltammetric signal. The quantitative analysis of pyrimidine were performed under the optimal conditions and the DPV curves toward various concentrations of pyrimidine were showed in Fig. 5 Detection of T/C in their blend solution were studied when the concentration of one substance maintained constant while another substance changed. In Fig. 5a, it is clearly observed that the electricity value exhibits a rising trend with increasing concentration of analyte, and in Fig. 5b, c has the same situation with T. The calibration plot is shown in this relationship between concentration and current values. For concentrations of T/C in the range from 1 to 4000/1 to 3000 μM, the linear regression equation can be depicted as: $I_{pa(T)} = 0.0060\ c + 0.08$ (r = 0.999)/$I_{pa(C)} = 0.0060\ c + 0.04$ (r = 0.999). The both detection limits of C and T (3S/N) are 0.2 μM. Figure 6 was the DPVs of T and C with different concentrations on the $WO_2$/W@C/GCE. The peak currents of T and C increased with the increasing of their concentrations from 1 to 3500 μM and 1 to 2700 μM, and the linear regression equation are: $I_{pa(T)} = 0.0060\ c + 0.07$ (r = 0.998) and $I_{pa(C)} = 0.0057\ c + 0.06$ (r = 0.999), which are close to the above results. It indicates that the method proposed in this paper could realize simultaneous determination for T and C.

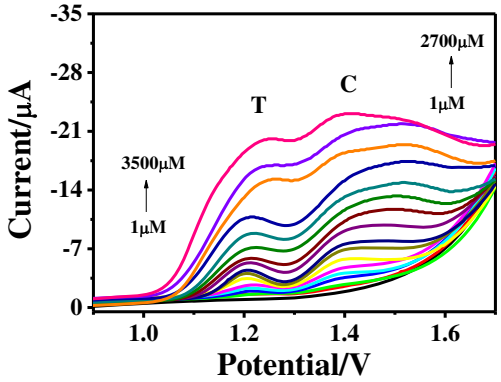


**Fig. 6** DPV of T/C with different concentrations in 0.2 M PB (pH 5.5). (Concentrations of T from 1, 10, 25, 50, 80, 160, 240, 320, 480, 640, 960, 1280, 1600, 2200, 2800 to 3500 μM, Concentrations of C from 1, 10, 25, 50, 80, 160, 240, 320, 480, 640, 960, 1280, 1600, 2200, 2500 to 2700 μM)

## Reproducibility, stability and interferences

The influence of several possible interference substances toward two targets oxidation peak current were examined in the PB containing 100 μM T and C. The tolerance limit is defined as the maximum concentration of foreign matter that can

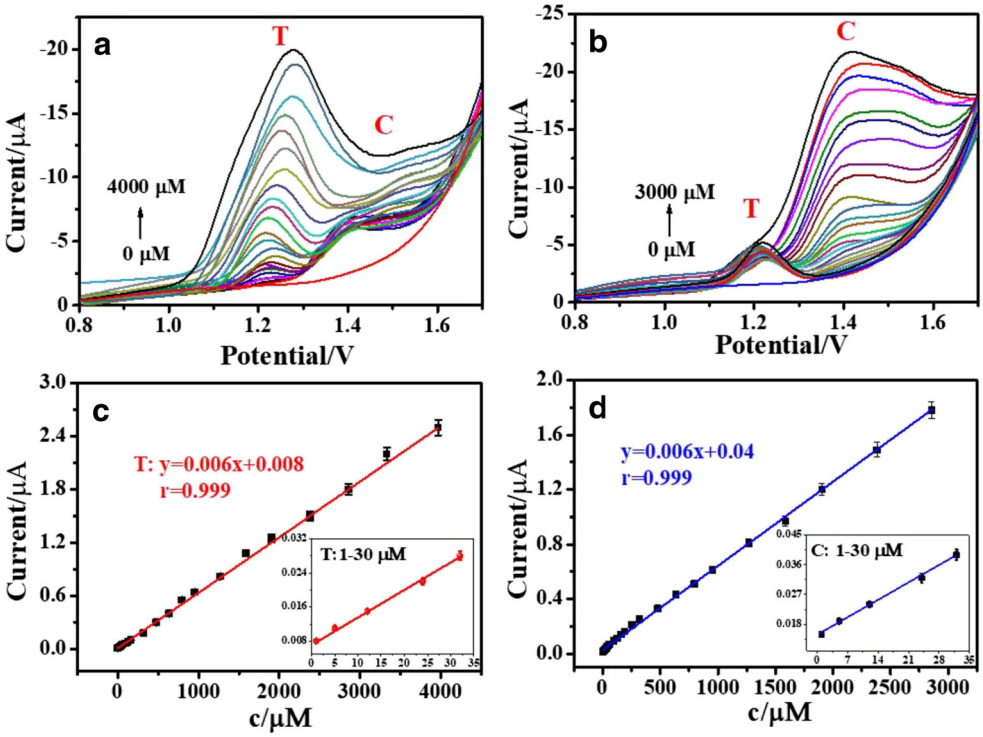


**Fig. 5** (**a**) DPV in 0.2 M PB (pH 5.5) at different concentrations of T at the potential of 1.26 V from 1, 5, 12, 24, 32, 40, 55, 95, 125, 160, 320, 480, 640, 800, 960, 1280, 1600, 1900, 2400, 2800, 3300 to 4000 μM; (**b**) C at the potential of 1.44 V from 1, 5, 12, 24, 32, 40, 55, 95, 125, 160, 200, 260, 320, 480, 640, 800, 960, 1260, 1560, 1960, 2400, 2800 to 3000 μM; (**c**) and (**d**) the related calibration plot

**Table 1** Comparison of analytical property to various modified electrodes

| Electrode | Linear range (μM) | | Detection limit (μM) | | Sensitivity (μA/cm$^2$ μM) | | Reference |
|---|---|---|---|---|---|---|---|
| | T | C | T | C | T | C | |
| MCF/GCE | 25–900 | 50–1500 | 24.00 | 27.00 | 16.6 | 16.6 | 8 |
| Nano-ZSM-5 BMIM | 50–1000 | 50–1000 | 10.70 | 13.80 | 0.016 | 0.021 | 9 |
| PANI/$MnO_2$/GCE | 10–100 | 10–100 | 1.30 | 1.30 | 1.5 | 2.4 | 21 |
| $Fe_3O_4$/MIM | 50–1200 | 50–1200 | 12.4 | 6.4 | 0.6 | 0.75 | 22 |
| Glassy carbon electrode | 1–20 | 1–20 | 0.89 | 1.76 | 5.04 | 3.35 | 34 |
| $WO_2$/W@C | 1–4000 | 1–3000 | 0.2 | 0.2 | 5.8 | 5.8 | This work |

induce a roughly ±5% relative error in the test. The tolerated ratios of foreign matter were 1:800 for $Zn^{2+}$, $Cu^{2+}$and $Ca^{2+}$, 1:500 for $Na^+$, $Mg^{2+}$ and $K^+$, 1:200 for glucose, sucrose, L-glutamic acid, 1:50 for adenine, guanine, uric acid, 1:15 for dopamine, ascorbic acid. The results indicated that the peak current of T and C were not significantly affected by the presence of common coexisting species, suggesting an excellent selectivity and great anti-interference ability of the $WO_2$/W@C/GCE and the method can be applied to evaluate T and C in real samples. We think the anti-interference capability will be more ideal, if the overpotential of T and C on $WO_2$/W@C/GCE can be further reduced, and the sensor will be used in more complex sample. Thus, to further reduce the overpotential become our focuses in the future research.

The reproducibility experiment was investigated based on $WO_2$/W@C/GCE with T and C mixed solution by DPV. The relative standard deviations (RSDs) for T and C analysis are calculated as 4.3% and 4.5% for six various electrodes in the same environment, respectively. The stability was assessed on $WO_2$/W@C/GCE, the $WO_2$/W@C/GCE was stored in a cold freezer for two weeks and test their effects. Experimental results show that there is no significant decline and the current value reach more than 95% of the original, demonstrating that the $WO_2$/W@C/GCE possess an unexceptionable stability. The above experimental results show that $WO_2$/W@C/GCE possesses satisfactory and excellent stability and reproducibility for practical application.

## Sample analysis

In order to evaluate the performance of $WO_2$/W@C/GCE for practical analysis, urine-1, urine-2, serum-1 and serum-2 were chosen as real samples. We adopted standard addition method within the scope of the standard curve based on $WO_2$/W@C/GCE and a known quantity of T/C was added. The result was listed in Table S1, the recoveries are in the range of 97.3% to 105.0% for different concentrations of two analytes. The result explains the feasibility of the method for detecting T and C in actual samples. Other reported methods compared with the our method about detecting T and C are listed in Table 1, which indicates that the method possesses wide linear range and high sensitivity.

## Conclusions

A new strategy was provided to construct the $WO_2$/W@C as modified electrode material with high electro-catalytic activity toward electrochemical oxidation of T and C, the forming process of $WO_2$/W@C were characterized in detail. Such preeminent electrochemical performances certify that the well-dispersed embedding of $WO_2$/W nanoparticles, porous channel, the presence of OVs and multiporous nanostructures are an efficient way to enhance the performance of $WO_2$/W@C electrode. The sensor shows better stability, reproducibility and anti-interference. Furthermore, it has been successfully applied for the analysis of T and C in human urine and blood serum samples, satisfactory results demonstrate that $WO_2$/W@C is a potential sensing material for the analysis of T and C in the real life. But the feasibility of the method for determination T/C in other complex sample is still underway due to their high overpotential.

**Acknowledgements** This project was supported by the National Nature Science Foundation of China (NSFC51672116), Science and technology foundation of ocean and fisheries of liao ning province (201408, 201406).

## References

1. Li H, Wang X, Wang Z, Zhao W (2016) Simultaneous determination of guanine, adenine, thymine and cytosine with a simple electrochemical method. J Solid State Electrochem 20(8):2223–2230. https://doi.org/10.1007/s10008-016-3227-2
2. Wei Y, Huang Q-A, Li M-G, Huang X-J, Fang B, Wang L (2011) CeO2 nanoparticles decorated multi-walled carbon nanotubes for electrochemical determination of guanine and adenine. Electrochim Acta 56(24):8571–8575. https://doi.org/10.1016/j.electacta.2011.07.048
3. Gill BD, Indyk HE (2007) Development and application of a liquid chromatographic method for analysis of nucleotides and nucleosides in milk and infant formulas. Int Dairy J 17(6):596–605. https://doi.org/10.1016/j.idairyj.2006.08.001

4. Erbao L, Bingchun X (2006) Flow injection determination of adenine at trace level based on luminol-K2Cr2O7 chemiluminescence in a micellar medium. J Pharm Biomed Anal 41(2):649–653. https://doi.org/10.1016/j.jpba.2005.12.012
5. Ensafi AA, Heydari-Bafrooei E, Amini M (2012) DNA-functionalized biosensor for riboflavin based electrochemical interaction on pretreated pencil graphite electrode. Biosens Bioelectron 31(1):376–381. https://doi.org/10.1016/j.bios.2011.10.050
6. Gao F, Fan T, Ou S, Wu J, Zhang X, Luo J, Li N, Yao Y, Mou Y, Liao X, Geng D (2018) Highly efficient electrochemical sensing platform for sensitive detection DNA methylation, and methyltransferase activity based on Ag NPs decorated carbon nanocubes. Biosens Bioelectron 99:201–208. https://doi.org/10.1016/j.bios.2017.07.063
7. Wang P, Wu H, Dai Z, Zou X (2011) Simultaneous detection of guanine, adenine, thymine and cytosine at choline monolayer supported multiwalled carbon nanotubes film. Biosens Bioelectron 26(7):3339–3345. https://doi.org/10.1016/j.bios.2011.01.011
8. Ren S, Wang H, Zhang H, Yu L, Li M, Li M (2015) Direct electrocatalytic and simultaneous determination of purine and pyrimidine DNA bases using novel mesoporous carbon fibers as electrocatalyst. J Electroanal Chem 750:65–73. https://doi.org/10.1016/j.jelechem.2015.05.020
9. Kaur B, Srivastava R (2014) Synthesis of ionic liquids coated nanocrystalline zeolite materials and their application in the simultaneous determination of adenine, cytosine, guanine, and thymine. Electrochim Acta 133:428–439. https://doi.org/10.1016/j.electacta.2014.04.019
10. Yin H, Zhu J, Chen J, Gong J, Nie Q (2018) MOF-derived in situ growth of carbon nanotubes entangled Ni/NiO porous polyhedrons for high performance glucose sensor. Mater Lett 221:267–270. https://doi.org/10.1016/j.matlet.2018.03.156
11. Wei W, Dong S, Huang G, Xie Q, Huang T (2018) MOF-derived Fe2O3 nanoparticle embedded in porous carbon as electrode materials for two enzyme-based biosensors. Sensors Actuators B Chem 260:189–197. https://doi.org/10.1016/j.snb.2017.12.207
12. Zhang L, Dou Y, Guo H, Zhang B, Liu X, Wan M, Li W, Hu X, Dou S, Huang Y, Liu H (2017) A facile way to fabricate double-shell pomegranate-like porous carbon microspheres for high-performance Li-ion batteries. J Mater Chem A 5(24):12073–12079. https://doi.org/10.1039/c7ta02415k
13. Zhu G, Wang L, Lin H, Ma L, Zhao P, Hu Y, Chen T, Chen R, Wang Y, Tie Z, Liu J, Jin Z (2018) Walnut-like multicore-Shell MnO encapsulated nitrogen-rich carbon Nanocapsules as anode material for long-cycling and soft-packed Lithium-ion batteries. Adv Funct Mater 28(18):1800003. https://doi.org/10.1002/adfm.201800003
14. Yang L, Zhang Y, Liu X, Jiang X, Zhang Z, Zhang T, Zhang L (2014) The investigation of synergistic and competitive interaction between dye Congo red and methyl blue on magnetic MnFe2O4. Chem Eng J 246:88–96. https://doi.org/10.1016/j.cej.2014.02.044
15. Liu X, Qi X, Zhang L (2018) 3D hierarchical magnetic hollow sphere-like CuFe2O4 combined with HPLC for the simultaneous determination of Sudan I-IV dyes in preserved bean curd. Food Chem 241:268–274. https://doi.org/10.1016/j.foodchem.2017.08.113
16. Tong Y, Liu X, Zhang L (2019) Green construction of Fe3O4@GC submicrocubes for highly sensitive magnetic dispersive solid-phase extraction of five phthalate esters in beverages and plastic bottles. Food Chem 277:579–585. https://doi.org/10.1016/j.foodchem.2018.11.021
17. Liu X, Liu M, Zhang L (2018) Co-adsorption and sequential adsorption of the co-existence four heavy metal ions and three fluoroquinolones on the functionalized ferromagnetic 3D NiFe2O4 porous hollow microsphere. J Colloid Interface Sci 511:135–144. https://doi.org/10.1016/j.jcis.2017.09.105
18. Zhu C, Fu S, Du D, Lin Y (2016) Facilely tuning porous NiCo2 O4 Nanosheets with metal valence-state alteration and abundant oxygen vacancies as robust Electrocatalysts towards water splitting. Chemistry 22(12):4000–4007. https://doi.org/10.1002/chem.201504739
19. Li Y, Wang H, Li Y, Wang Q, Li D, Wang R, He B, Gong Y (2018) 2D metal–organic-framework array-derived hierarchical network architecture of cobalt oxide flakes with tunable oxygen vacancies towards efficient oxygen evolution reaction. J Catal 364:48–56. https://doi.org/10.1016/j.jcat.2018.05.006
20. Wu HB, Xia BY, Yu L, Yu XY, Lou XW (2015) Porous molybdenum carbide nano-octahedrons synthesized via confined carburization in metal-organic frameworks for efficient hydrogen production. Nat Commun 6:6512. https://doi.org/10.1038/ncomms7512
21. Anu Prathap MU, Srivastava R, Satpati B (2013) Simultaneous detection of guanine, adenine, thymine, and cytosine at polyaniline/MnO2 modified electrode. Electrochim Acta 114:285–295. https://doi.org/10.1016/j.electacta.2013.10.064
22. Kaur B, Srivastava R (2014) Ionic liquids coated Fe3O4 based inorganic-organic hybrid materials and their application in the simultaneous determination of DNA bases. Colloids Surf B: Biointerfaces 118:179–187. https://doi.org/10.1016/j.colsurfb.2014.03.020
23. Shu C, Kang S, Jin YH, Yue X, Shen PK (2017) Bifunctional non-precious metal Electrocatalysts of porous $WO_2$ hexahedral networks for full water splitting. J Mater Chem A 5:9655–9660. https://doi.org/10.1039/C7TA01527E
24. Elias L, Cao P, Hegde C (2016) Magnetoelectrodeposition of Ni-W alloy coatings for enhanced hydrogen evolution reaction. RSC Adv 6:111358–111365. https://doi.org/10.1039/C6RA23944G
25. Wang G, Sun H, Ding L, Zhou G, Wang ZS (2015) Growth of cu particles on $Cu_2O$ truncated octahedron: tuning of the cu content for efficient glucose sensing. Phys Chem Chem Phys 17:24361–24369. https://doi.org/10.1039/C5CP03748D
26. Xiao Y, Zheng L, Cao M (2015) Hybridization and pore engineering for achieving high-performance lithium storage of carbide as anode material. Nano Energy 12:152–160. https://doi.org/10.1016/j.nanoen.2014.12.015
27. Wang Y, Guo X, Wang Z, Lü M, Wu B, Wang Y, Yan C, Yuan A, Yang H (2017) Controlled pyrolysis of MIL-88A to Fe2O3@C nanocomposites with varied morphologies and phases for advanced lithium storage. J Mater Chem A 5(48):25562–25573. https://doi.org/10.1039/c7ta08314a
28. Xu X, Liu J, Liu Z, Shen J, Hu R, Liu J, Ouyang L, Zhang L, Zhu M (2017) Robust Pitaya-structured pyrite as high energy density cathode for high-rate Lithium batteries. ACS Nano 11(9):9033–9040. https://doi.org/10.1021/acsnano.7b03530
29. Zhang K, Yang H, Lü M, Yan C, Wu H, Yuan A, Lin S (2018) Porous MoO2-cu/C/Graphene nano-octahedrons quadruple nanocomposites as an advanced anode for lithium ion batteries with enhanced rate capability. J Alloys Compd 731:646–654. https://doi.org/10.1016/j.jallcom.2017.10.091
30. Cao L, Li Y, Wu J, Li W, Huang J, Feng Y, Yao C, Li J, Wang R, Kang Q, Feng L (2018) Facile synthesis of carbon coated MoO3 nanorods decorated with WO2 nanoparticles as stable anodes for lithium-ion batteries. J Alloys Compd 744:672–678. https://doi.org/10.1016/j.jallcom.2018.02.112
31. Shifu C, Lei C, Shen G, Gengyu C (2005) The preparation of coupled WO3/TiO2 photocatalyst by ball milling. Powder Technol 160(3):198–202. https://doi.org/10.1016/j.powtec.2005.08.012

32. Anson FC (1964) Application of Potentiostatic current integration to the study of the adsorption of CobaIt(lll)-( Ethylenedinitri1o)tetraacetate on mercury electrodes. Anal Chem 36:932–934
33. Gumpu MB, Veerapandian M, Krishnan UM, Rayappan JB (2017) Simultaneous electrochemical detection of cd(II), Pb(II), as(III) and hg(II) ions using ruthenium(II)-textured graphene oxide nanocomposite. Talanta 162:574–582. https://doi.org/10.1016/j.talanta.2016.10.076
34. Oliveira-Brett AM, Piedade JAP, Silva LA, Diculescu VC (2004) Voltammetric determination of all DNA nucleotides. Anal Biochem 332:321–329. https://doi.org/10.1016/j.ab.2004.06.021